

Reduction of early-time perturbation growth in ablatively driven laser targets using tailored density profiles

Nathan Metzler

Physics Department, Nuclear Research Center Negev, P. O. Box 9001, Beer Sheva, Israel

Alexander L. Velikovich

Berkeley Research Associates, Inc., Springfield, VA 22150

John H. Gardner

LCP&FD, Naval Research Laboratory, Washington, D.C. 20375

Abstract

We investigate analytically and numerically the effects of tailoring the density profile in a laser target in order to decrease imprinting of mass perturbations due to the long-wavelength modes. Inverting the acceleration of the ablation front during the shock transit time could reduce the early-time mass perturbation amplitudes developed in the target after the shock transit. This principle was first suggested for mitigating the RT instability of imploding Z-pinches [Velikovich *et al.*, Phys. Rev. Lett. **77**, 853 (1996); Phys. Plasmas **5**, 3377 (1998)]. As the shock wave slows down propagating into higher density layers, the effective gravity near the ablation front has the same direction as the density gradient. This makes the mass perturbations near it oscillate at a higher frequency and at a lower amplitude than they normally would due to the “rocket effect” caused by mass ablation [Sanz, Phys. Rev. Lett. **73**, 2700 (1994); Piriz *et al.*, Phys. Plasmas **4**, 1117 (1997)]. So, tailoring density profiles instead of using flat densities is demonstrated to reduce the “seed” mass perturbation amplitude at the onset of the exponential RT growth.

PACS numbers: 52.40.Nk, 52.35.Py

I. INTRODUCTION.

A critical issue of direct-drive laser fusion program is mitigating the distortion of the imploded pellet due to the Rayleigh-Taylor (RT) instability.¹ The common approach is to deal directly with the initial sources of the instability. Advances in improving optical smoothing of laser beams and developing the pellet manufacturing technologies reduce the seed for the ablative RT instability to a very low level. Still, even a small perturbation seed could be large enough to preclude the achievement of high gain in the implosion.

To complement the two above direct means to the RT seed reduction, consider the following approach. Suppose that the sources of mass perturbations, that is, the levels of the beam and target non-uniformity, are given. Let us try to determine the structure of the pellet that minimizes the seed for the RT instability produced by these two sources. Here, we limit ourselves to the relatively simple case of structuring the target via radial density tailoring. The high gain implosion regime imposes certain requirements on the thickness and the areal mass of the pellet, and the laser pulse shape. We have to find a way to distribute the given mass within a layer of a given thickness (that is, the way the density profile $\rho(r)$ should be tailored) in order to minimize the early-time mass perturbation amplitude. In general, the search for the most perturbation-resistant pellet structure could include tailoring of both density and material composition, as well as adjusting the laser pulse shape to the density/material structure.

It is known^{2,3} that the fastest classical RT mode is localized near the accelerated surface, and its growth rate is not sensitive to the density profile in the fluid. There are some indications⁴ that density tailoring can help mitigate the target distortion due to the exponential RT instability development, but this is not the effect studied here. In the present paper, we concentrate on the early-time perturbation growth preceding the exponentiation phase. As shown from recent studies,⁵⁻⁷ the evolution of perturbations at early times resembles the development of vorticity-driven Richtmyer-Meshkov (RM) instability rather than the acceleration-driven RT instability. The mass ablation turns out to be a sufficiently strong stabilizing effect to stop the RM-like perturbation growth at all wavelengths (in contrast with the RT growth, which is only stabilized at sufficiently short wavelengths¹). Due to the “rocket effect” caused by mass ablation,^{8,9} mass perturbations instead of growing linearly exhibit decaying oscillations. These oscillations, discussed in connection with ablative RT instability^{8,9}, were first observed in numerical simulations of early-time mass perturbation growth.^{1,5,6} They have been described by the analytical model of Ref. 7. The initial surface roughness and laser beam non-uniformity evolve during the shock transit time into mass perturbations. These mass perturbation amplitudes seed the RT growth, once the rarefaction wave from the rear side of the target reaches the ablation front and the subsonic acceleration of the target begins.

The role of density tailoring stems from the possibility to invert the acceleration of the unstable interface during the shock transit time. If a shock wave is driven into increasing density,

and slows down as it propagates, the ablation front that follows the shock front would be decelerated, too. Hence, local gravity is in the same direction as the density gradient, and small perturbations tend to oscillate (propagate as running gravitational waves along the accelerated interface) rather than growing exponentially. This mechanism contributes to the oscillations additionally to the “rocket effect” mentioned above. Consequently, it affects the early-time evolution of perturbations by increasing characteristic frequencies of their oscillations. For a given level of non-uniformity supplying the initial perturbations (e. g., lateral variation of laser intensity), increased oscillation frequencies imply lower mass perturbation amplitudes at the onset of the exponential RT growth.

Use of tailored density profiles for stabilization was recently proposed to mitigate the RT instability development in imploding Z-pinch^{10,11}. As far as the perturbation growth is concerned, the main difference between the laser-driven ablative acceleration and the electromagnetic plasma acceleration in a Z-pinch¹⁰ is the purpose, and, by inference, the regime of acceleration. In a Z-pinch plasma radiation source (PRS), the plasma is accelerated in order to convert its kinetic energy into thermal at stagnation, and finally into radiation. Thus, the shock transit time might include all or most of the implosion, as is the case for uniform fill or thick annular cylindrical loads. A shock-driven acceleration is not feasible in direct drive laser fusion - too much pellet preheat prevents fuel compression. The opportunity to affect the perturbation growth using the density tailoring is therefore limited to the early time, while the shock and compressibility effects are still relevant. Therefore, the ablation drive case requires a much more detailed study of the perturbation evolution.

As demonstrated below, the radial density tailoring affects perturbations whose wavelengths are of order of, or less than the shell thickness. At early time, while the aspect ratio is large, the spherical pellet is nearly planar for these perturbations. Therefore, in the present paper we study the case of a planar geometry. This choice somewhat simplifies both analysis and numerics, but in no way reduces the generality of the result. The stabilizing effect would work in the same way for spherical geometry as it does for planar or cylindrical¹⁰ cases.

The paper is structured as follows. In Section II, we describe the dynamics of a shock wave driven by an increasing ablation pressure into a tailored density profile, compare the 1-D simulation results to the exact self-similar solution, and make analytical estimates for the evolution of perturbations. Section III presents a numerical study of the perturbation evolution for the various types of density tailoring, and Section IV concludes with a discussion.

II. THEORY

A. Self-similar unperturbed flows

Let us describe one-dimensional (1-D) gas dynamics of a shock-piston flow generated when a shock wave is driven into a tailored density profile by a pressure that either remains constant or increases with time. The piston could be visualized as an ablation front for laser acceleration, or as the magnetic field/plasma interface, in a Z-pinch.¹⁰ We will find how the piston acceleration (in the

x direction) depends on the relation between the rate of pressure increase and the shape of the tailored density profile. Typically, the plasma represents a “heavy fluid”, accelerated by the pressure of a “light fluid”, whether it be a low-density ablated plasma or a massless magnetic field, which gives rise to the RT instability. However, the presence of a tailored density profile in a shock-piston situation could reverse the direction of acceleration. In particular, if the pre-shock density increases with time faster than the post-shock pressure, the interface accelerates opposite to the propagation direction of the shock wave. During this time, the propagating shock wave keeps bringing new layers of the initially resting gas into motion in the positive x direction. This has been previously shown heuristically, using a 0-D snowplow model.¹⁰ In this Section, we will demonstrate the same in a more rigorous way, with the aid of an exact self-similar solution, generalizing that obtained in Ref. 12 and, in a slightly different form, in Ref. 13. Evolution of small perturbations on top of this self-similar flow will be studied below – analytically in Section IIB and numerically in Section III.

Consider a half-space $x > 0$ filled with an ideal gas whose density profile is tailored according to a power law: $\rho(x) = \rho_0(x/\Delta)^\chi$, where ρ_0 and Δ are dimensional normalization constants, and the constant dimensionless exponent $\chi > -1$ determines the shape of the profile. Let a piston, which moves according to the power law

$$x_p(t) \equiv L(t) = g_0 t^m / m \quad (1)$$

(here again, g_0 is a dimensional normalization constant, m is a dimensionless exponent) drive a shock wave into the gas. In the reference frame where the piston is at rest, the 1-D motion of the shocked fluid is described by the equations of continuity, adiabaticity, and motion:

$$\left(\frac{\partial}{\partial t} + u \frac{\partial}{\partial x} \right) \ln \rho + \frac{\partial u}{\partial x} = 0, \quad (2)$$

$$\left(\frac{\partial}{\partial t} + u \frac{\partial}{\partial x} \right) \ln p + \gamma \frac{\partial u}{\partial x} = 0, \quad (3)$$

$$\left(\frac{\partial}{\partial t} + u \frac{\partial}{\partial x} \right) u + \frac{1}{\rho} \frac{\partial p}{\partial x} = -(m-1) g_0 t^{m-2}, \quad (4)$$

where u , ρ , p , and γ are the x -velocity, density, pressure, and adiabatic exponent of the shocked gas, respectively. For $m > 1$, both the shock and the piston accelerate with time, so that local gravity has negative direction, from the accelerated fluid to the piston. For $m < 1$, the shock and the piston decelerate, and the local gravity is positive, directed from the piston to the fluid.

If the pre-shocked gas is cold, so that the shocks wave is strong at all time, then Eqs. (2)-(4) admit an exact self-similar solution. Introducing a self-similar variable, $\eta = x / L(t)$, we use the self-similarity ansatz

$$\begin{aligned} u(x, t) &= \dot{L}(t) U(\eta) = g_0 t^{m-1} U(\eta), \\ \rho(x, t) &= \rho_0 L(t)^\chi N(\eta) = \rho_0 (g_0 / m)^\chi t^{m\chi} N(\eta), \\ p(x, t) &= \rho_0 L(t)^\chi \dot{L}^2 P(\eta) = \rho_0 (g_0^{\chi+2} / m^\chi) t^{2m-2+m\chi} P(\eta), \end{aligned} \quad (5)$$

where $U(\eta)$, $N(\eta)$, and $P(\eta)$ are dimensionless functions representing the self-similar profiles of velocity, density, and pressure, respectively. With the aid of (5), the gasdynamic equations (2)-(4) are reduced to a system of two ordinary differential equations, which has to be solved numerically, as described in Appendix I.

As seen from Eq. (5), this solution is generated if the pressure at the piston is related to either distance traveled by the piston or to time by a power law, e. g., $p_p(t) \propto t^\sigma$. Comparing this to (5), we find the value of m that corresponds to σ for a given χ :

$$m = \frac{\sigma + 2}{\chi + 2}. \quad (6)$$

Equation (6) illustrates that the shock-piston flow accelerates the fluid when the pressure at the piston rises faster than the density in the unperturbed fluid: $m > 1$ when $\sigma > \chi$. Otherwise, when $\sigma < \chi$, the fluid is decelerated ($m < 1$). For instance, if the pressure rises linearly, $\sigma = 1$, then the plasma layer of parabolic density ($\chi = 2$) will be decelerated: $m = 3/4$. If the same linearly rising pressure drives a uniform density profile ($\chi = 0$), then the pre-shock density increases slower than the post-shock pressure does, which means acceleration: $m = 3/2$.

The self-similar profiles of post-shock density and temperature in an ideal gas with $\gamma = 5/3$ for these two cases are shown in Fig. 1. The density profile near the piston, at $\eta \ll 1$, has the power-law asymptotic shape

$$N(\eta) \sim \eta^s, \quad \text{where} \quad s = \frac{\chi m(\gamma - 1) - 2(m - 1)}{m(\gamma + \chi + 2) - 2}, \quad (7)$$

which is typically sharper than the pre-shock profile. Since the pressure at $\eta \rightarrow 0$ must be of order unity ($P(\eta) \sim \eta^0$), we find for the self-similar temperature profile: $\Theta(\eta) \equiv P(\eta) / N(\eta) \sim \eta^{-s}$. For the above two cases, $\sigma = 1$, $\chi = 0$ and 2 , we find from (7): $s = -2/7$ and $2/3$, respectively. Then the temperature vanishes and the density diverges near the accelerated piston ($\chi = 0$, $m = 3/2$), and vice versa, the temperature diverges and the density vanishes near the decelerated piston ($\chi = 2$, $m = 3/4$), cf. Figs. 1 (a), (b). This is not surprising. The entropy of the fluid particles adjacent to the piston is determined at $t \rightarrow 0$, when the shock wave is formed. For $m = 3/2$, the shock velocity in this limit tends to zero, and so do the post-shock temperature and pressure. The isentropic compression that follows can make the pressure in these fluid particles finite only via infinite increase of density. Conversely, for $m = 3/4$, the shock velocity in the limit $t \rightarrow 0$ diverges, and so does the post-shock temperature. Due to the subsequent isentropic compression, the temperature there remains infinite afterwards.

Figure 2 presents a comparison of the self-similar density profile calculated for the case of decelerated piston ($\sigma = 1$, $\chi = 2$, $m = 3/4$) with those obtained in our simulations for similar conditions. The simulated density profiles are seen to remain self-similar during the shock transit time. The density gradient near the ablative piston in simulation is less steep than in the analytical solution, because the temperature rises even faster than in Fig. 1(a), the ablation pressure being

maintained primarily through the conductive heat flow from the corona. Also, in the computations the density at $x = 0$ is finite. Nevertheless, the observed self-similarity supports our prediction that the ablation front in this case is decelerated, as shown below in Section III.

B. Simple linear stability analysis

Now we assume that the piston driving the self-similar flow is an ablation front. Then the driving pressure is created by a mass ablation through this front, so that we deal with a “leaky piston” rather than a solid piston or a contact interface. Still, the self-similar solution of Section II.A could be valid, once the ablation front is identified with some surface $\eta = \eta_a = \text{const}$ rather than with the surface $\eta = 0$. Then the ablation velocity v_a , like all the characteristic velocities, is proportional to $\dot{L} = mL/t$, where L is the distance traveled by the piston, see Eqs. (1), (5). We introduce a dimensionless constant v characteristic of the ablation rate:

$$v = \frac{v_a}{mL/t}. \quad (8)$$

Let us describe perturbations of the ablation front using a discontinuity model identical to that of Piriz *et al.*⁹ The model involves another dimensionless characteristic of the ablation front, the density ratio $r_D = \rho_2 / \rho_1$, where the subscripts 1 and 2 refer to the dense shocked plasma ahead of and to the low-density plasma behind the ablation front, respectively. This parameter is also supposed to be constant in time. Typically, $r_D < 1$, so that the Atwood number across the ablation front, $A = (1 - r_D) / (1 + r_D)$, is close to unity. We modify the boundary conditions given in Ref. 9 for the case of time-dependent acceleration and ablation velocity, and require all the perturbations to be localized near the ablation front or propagating from it, upstream or downstream. Then the solution of the perturbation problem contains no perturbations incident on the front, only waves outgoing from it. As shown in Appendix II, the boundary conditions in this case are reduced to

$$\frac{d}{dt} \delta x_a + k v_a \delta x_a - \delta v_x = 0, \quad (9)$$

$$\frac{d}{dt} \delta v_x + \frac{3 - r_D}{1 + r_D} k v_a \delta v_x + A \left[\frac{1 - r_D}{r_D} k^2 v_a^2 - gk \right] \delta x_a = 0, \quad (10)$$

where δx_a is the displacement amplitude of the ablation front, δv_x is the perturbation of the axial velocity at the ablation front, k is the perturbation wave number. The boundary condition (9) at the ablation front is well known in the literature,¹⁴ the boundary condition (10) is derived in Appendix II from the results of Ref. 9 under the above assumptions.

Introduce a new dimensionless independent variable [not to be confused with one of the dependent variables, self-similar temperature $\Theta(\eta)$]

$$\theta = kL(t) = kg_0 t^m / m. \quad (11)$$

Substitution of (8), (11) and $kg(t) = m(m-1)\theta / t^2$ into Eqs. (9), (10) reduces this system to a single equation for δx_a :

$$\theta \frac{d^2}{d\theta^2} \delta x_a + \left(\frac{4v\theta}{1+r_D} + \frac{m}{m-1} \right) \frac{d}{d\theta} \delta x_a + \left[\frac{v^2\theta}{r_D} + \frac{(m-1)(v-A)}{m} \right] \delta x_a = 0. \quad (12)$$

Solutions of this equation are expressed via the confluent hypergeometric functions. In particular, the solution regular at $t = 0$ and satisfying the initial condition $\delta x_a(t=0) = \delta x_0$ is given by

$$\frac{\delta x_a}{\delta x_0} = \exp \left[-v \left(\frac{2}{1+r_D} + \frac{iA}{\sqrt{r_D}} \right) \theta \right] {}_1F_1 \left(\frac{(m-1)}{m} \left[1 - \frac{i(v+1)\sqrt{r_D}}{v} \right], \frac{m-1}{m}, \frac{2ivA}{\sqrt{r_D}} \theta \right), \quad (13)$$

where ${}_1F_1(a, c, z)$ is the Kummer's function.¹⁵

To analyze the properties of this solution, let us start with the simple case of negligible effect of mass ablation, obtained from (13) in the limit $v \rightarrow 0$. In this limit, the Kummer's function is reduced to the Bessel function (Ref. 15, Eq. 13.5.13):

$$\frac{\delta x_a}{\delta x_0} = \Gamma \left(\frac{m-1}{m} \right) \left[\frac{(1-m)A\theta}{m} \right]^{1/2m} J_{-1/m} \left(2\sqrt{\frac{(1-m)A\theta}{m}} \right). \quad (14)$$

Since $A > 0$, the evolution of perturbations is determined primarily by the sign of $1-m$, that is, by the direction of acceleration of the interface. If $m < 1$, so that the interface is decelerated, and there is no reason for the RT instability to develop, then the argument of the Bessel function in (14) is real. At late time ($\theta \gg 1$), the perturbations oscillate:

$$\frac{\delta x_a}{\delta x_0} \sim \frac{1}{\sqrt{\pi}} \Gamma \left(\frac{m-1}{m} \right) \left[\frac{(1-m)A\theta}{m} \right]^{\frac{2-m}{4m}} \cos \left(2\sqrt{\frac{(1-m)A\theta}{m}} + \frac{\pi}{2m} - \frac{\pi}{4} \right). \quad (15)$$

The amplitude of oscillations, as seen from Eq. (15), is slowly growing. A qualitative explanation of this is found in Ref. 10: amplitude of a pendulum oscillating in a slowly decreasing gravitational field increases.

For $m > 1$, the interface is accelerated, and therefore, is RT unstable. In this case, in Eq. (14) we have a modified Bessel function, which describes exponential growth instead of oscillations at late time:

$$\frac{\delta x_a}{\delta x_0} \sim \frac{1}{2\sqrt{\pi}} \Gamma \left(\frac{m-1}{m} \right) \left[\frac{(m-1)A\theta}{m} \right]^{\frac{2-m}{4m}} \exp \left(2\sqrt{\frac{(m-1)A\theta}{m}} \right) \quad (16)$$

For the particular case of constant acceleration ($m = 2$), Eq. (14) yields

$$\frac{\delta x_a}{\delta x_0} = \cosh(\sqrt{Agkt}), \quad (17)$$

as it should be. The perturbation growth described by Eq. (14) for the cases of $m = 3/4$ and $m = 3/2$ is shown in Fig. 3(a).

Introduction of mass ablation (finite v) changes the picture qualitatively. Now the asymptotic behavior of solution (13) at late time is¹⁵

$$\frac{\delta x_a}{\delta x_0} \sim \text{const} \cdot \theta^{\frac{1-m}{2m}} \text{Re} \left\{ \exp \left[-v \left(\frac{2}{1+r_D} + i \frac{A}{\sqrt{r_D}} \right) \theta + i \frac{(m-1)\sqrt{r_D}}{2mv} \ln \theta \right] \right\}. \quad (18)$$

The solution describes decaying oscillations for any sign of acceleration. It is qualitatively similar to the particularly simple case of zero acceleration [$m = 1, \theta = k v_0 t$, where v_0 for this case is an appropriate replacement of g_0 in the definition (1)]:

$$\frac{\delta x_a}{\delta x_0} = \exp\left(-\frac{2vk v_0 t}{1+r_D}\right) \cos\left(\frac{vA k v_0 t}{\sqrt{r_D}}\right), \quad (19)$$

cf. Ref. 7. The evolution of perturbations described by Eq. (13) for the cases of $m = 3/4$ and $m = 3/2$ and $v = 0.05$ is shown in Fig. 3(b). The only difference between the cases of acceleration ($m = 3/2$) and deceleration ($m = 3/4$) is that in the former case the perturbation amplitude reaches a higher peak value and oscillates at a lower frequency.

Stabilization of all modes in all acceleration regimes is explained with the aid of the dispersion relation obtained in Ref. 9 (self-consistent derivations of similar relations are found in Refs. 8, 16). The exponential growth rate for ablative RT instability is found to be equal to

$$\Gamma = \left(Agk - \frac{A^2}{r_D} k^2 v_a^2 \right)^{1/2} - \frac{2k v_a}{1+r_D}. \quad (20)$$

This expression follows from Eqs. (9), (10) if the ablation velocity and acceleration, v_a and g , are assumed constant. For the wavenumbers exceeding a cut-off value k_c , the instability is fully suppressed. Equation (20) demonstrates that the cut-off wavelength is determined by the balance of the two terms in parentheses,⁸ $k^2 v_a^2 / r_D > gk$, rather than by the balance of the whole term in parentheses and the second terms in the right-hand side of Eq. (20), $k v_a > \sqrt{gk}$, since $r_D \ll 1$. For k exceeding the cut-off value, Eq. (20) predicts exponentially decaying oscillations. Qualitatively, this stabilization mechanism is described in Ref. 9. It is based on the fact that the ablation front is an isotherm.¹⁷ When the front moves into a higher temperature area, its temperature therefore does not increase, but the temperature gradient near it does. Increased temperature gradient speeds up the mass ablation, producing the “rocket effect”⁹ responsible for the oscillations that tend to decrease the perturbation.

For our self-similar acceleration regimes, $k^2 v_a^2 \propto t^{2m-2}$, whereas $gk \propto t^{m-2}$. Since m is positive, $k^2 v_a^2$ grows with time faster than gk . If g is positive ($m > 1$, acceleration), then eventually $k^2 v_a^2 / r_D$ exceeds gk , and the exponential perturbation growth evolves into decaying oscillations. Otherwise, if g is negative ($m < 1$, deceleration), we have decaying oscillations from the start, see Eq. (20). This is exactly what is described by Eqs. (13), (18), (19), and illustrated by Fig. 3(b).

To summarize, we have predicted decaying oscillations instead of exponential perturbation growth for all wavelengths and all acceleration regimes subject to self-similarity restriction. This is a physically meaningful conclusion that could be tested in simulation and experiment. In contrast with that, neither the prediction of the exponential decay of perturbation, nor the calculated rates of decay should be taken very seriously. The reason is that our simplifying assumption that no external perturbations come to the ablation front as incident waves [see Eq. (A17)] is not fully justified.

Actually, the plasma that reaches the ablation front has first passed through the rippled shock front. The plasma particles therefore bring to the ablation front the perturbations of vorticity left after the shock passage. The incident perturbations also decay with time, but much slower than exponentially. For instance, in the case of zero acceleration ($m = 1$), the perturbations oscillate and decay as Bessel functions of time, that is, as $t^{-1/2}$ or $t^{-3/2}$, depending on whether the shock wave is strong or not.¹⁸ If the ablation front is RT unstable, then this power-law source of external perturbations does not change the exponential growth rate. This is why the incident perturbations could be safely neglected when the expressions for the growth rate like (20) are derived (if the resulting growth rate is positive). If there is no exponential RT growth, this approximation is no longer justified. Therefore, the exponential decay rates estimated above have little physical significance. Still, the corresponding oscillation frequencies are physically meaningful because they describe the immediate pressure response to the perturbation of the ablation front due to the “rocket effect”.⁹

The complicated early-time evolution of perturbations generates the seeds for the exponential RT instability development that starts after the shock transit time. We are interested in designing our target so that the given external perturbations (e. g., lateral non-uniformity of the laser beam) generate as small mass perturbation seeds as possible. This is where the tailored density profiles can help. Tailoring the initial density profile makes g negative from the start. As shown above [e. g., see Fig. 3(b)], this increases the frequency of oscillations of the ablation front and decreases the peak perturbation amplitude. We expect this effect to help decrease the perturbation amplitudes at the time when the RT instability starts to develop. Simulation results presented in the next Section demonstrate that this indeed could be done.

III. NUMERICAL SIMULATION

The simulations were performed in two dimensions (2-D) using the FAST hydrocode.¹⁹ This code has proved to be very robust over a wide range of problems, including reactive flows,²⁰ turbulent jets,²¹ flows about ship superstructure,²² and RT instabilities in inertial confinement fusion targets.²³ In the studies of the early-time perturbation growth in laser targets, the FAST code has proved effective at reproducing experimental observations of laser imprinting²⁴ and at predicting the oscillations due to the “rocket effect”.^{1,6} The code includes flux-corrected transport (FCT) advection,²⁵ inverse bremsstrahlung laser energy absorption (multiple ray trace), and Spitzer-Härm thermal conduction.²⁶ Radiation transport and tabulated equation of state (EOS) are also included in the code. These, however, have not been invoked in the simulations reported below. Our goal is to demonstrate the hydrodynamic effect of density tailoring alone, without any contribution of smoothing due to radiation transport or EOS effects. We simulate ablative acceleration of CH (plastic) targets.

We compare four target structures that differ mainly by their density profiles, see Fig. 4(a). [Note that in the simulations, the laser radiation comes from the positive x direction, accelerating the

target to negative x (the coordinate x emulates r in spherical geometry), a different sign from that chosen in Section II. This should not cause any confusion, since all the results of Section II are invariant under the substitution $x \leftrightarrow -x$.]

All the targets have the same areal mass $68.2 \mu\text{m g/cm}^3$. Targets 1 to 3 have also the same total thickness, $140 \mu\text{m}$. The front part of target 1 approximates the parabolic density profile of Section II ($\chi = 2$). Density profile starting from $\rho = 0$ is not realistic in target design, so that the actual density profile of target 1 is

$$\rho(x) = \rho_0 + (\rho_1 - \rho_0) \left(\frac{x}{\Delta} \right)^2, \quad (21)$$

where $\rho_0 = 0.05 \text{ g/cm}^3$ (a foam of this low density could be manufactured; this value is just about the critical density for KrF laser radiation), $\rho_1 = 1.07 \text{ g/cm}^3$ (solid plastic density), $\Delta = 120 \mu\text{m}$, followed by a $20 \mu\text{m}$ payload of solid plastic [we also did some runs for the initial density profile (21) without adding the payload]. In target 2, the areal mass contained in the profile (21) is uniformly distributed over the same thickness, $120 \mu\text{m}$, which corresponds to a uniform density $\rho = 0.39 \text{ g/cm}^3$, and followed by the same $20 \mu\text{m}$ payload. In target 3, the total mass $68.2 \mu\text{mg/cm}^3$ is uniformly distributed with the constant density $\rho = 0.487 \text{ g/cm}^3$, over the same total thickness, $120 \mu\text{m} + 20 \mu\text{m} = 140 \mu\text{m}$. Finally, the solid plastic target 4 has the same total mass, and, therefore, is $63.7 \mu\text{m}$ thick, that is, thinner than the other three.

The targets are driven by a $0.248 \mu\text{m}$ KrF laser radiation, as in Nike laser at the Naval Research Laboratory.²⁷ Two shapes of laser pulse are used. One is selected to provide in target 1 a linear increase of pressure from 0 to 4 Mbar during the shock transit through the density profile (21), that is, in the first 4 ns [Fig. 4(b)], after which the laser intensity is held constant. This pulse shape, as expected from the results of Section II and demonstrated in Fig. 5 below, at early time ($< 4 \text{ ns}$) produces a decelerating ablation front in target 1, and an accelerated ablation front in targets 2 to 4. The other laser pulse shape studied here is a constant incident laser intensity, which corresponds to the ablative pressure slowly decreasing from 2.75 Mbar to 1.75 Mbar at 10 ns due to increased absorption in the plasma corona. Here again, the ablation front in target 1 at early time must be decelerating. In other targets, however, we expect zero acceleration, or even a small deceleration (due to decreasing pressure). Of course, the theory of Section II does not extend to the situation after the shock wave breaks out at the rear surface of targets 1, 3, 4, or is reflected from the payload boundary of target 2. There is no analytical theory available to describe perturbation growth during the reverberation of shock and expansion waves, which eventually leads to the subsonic acceleration regime. Here, we have to rely on the simulation results.

To facilitate comparison between various cases, we introduce a constant single-mode lateral variation of the incident laser intensity. Evolution of perturbations studied below, therefore, corresponds to laser imprinting of mass perturbations. As explained in Ref. 6, the early-time perturbation growth due to the surface roughness is physically equivalent to that produced by the

laser imprint. The difference is only in the initial conditions: in the former case, we create initial amplitude of the perturbation, whereas in the latter we supply the perturbation with initial momentum. The perturbation growth that follows is governed by the same physics and could be scaled from one case to another. With tailored density profiles, the same amplitude of surface ripples would imply a 20-fold difference in the initial mass variation between targets 1 and 4. Below, we have all the targets initially uniform, driven by laser pulses with the same lateral intensity variation, so that the comparison between the targets is deemed fair. For each target/laser pulse shape combination, we run the code with single-mode perturbation wavelengths of 15 μm , 30 μm , and 60 μm .

Figure 5 is plotted for targets 1 (a) and 2 (b) driven by a linearly increasing ablative pressure. It shows the x - t trajectories of fluid particles, that give an idea about the motion of the ablation front. We see that at early time the ablation front in target 1 is indeed decelerated, as predicted in Section II.A. Similarly, we demonstrate that for all the other targets, the ablation front is accelerated by the linear pressure increase from the beginning of the laser pulse.

Figures 6 to 8 compare the evolution of mass perturbations between targets 1 to 4, all of them driven by a laser pulse with linearly increasing ablative pressure, and a 0.2% rms single-mode lateral intensity variation, $\lambda = 15 \mu\text{m}$, 30 μm , and 60 μm , respectively. Here, the early time (shock transit) corresponds to the first 4 ns, whereas the “late time”, when the RT instability of acceleration develops exponentially, starts somewhere between 6 and 8 ns.

For all cases, the qualitative behavior agrees with the predictions of Section II.B. The mass perturbations tend to oscillate, no matter whether the ablation front is accelerated or decelerated, although for the latter case (target 1) the frequency of oscillations is notably higher, and the amplitude lower. We even observe some [albeit non-exponential, cf. Fig. 3(b)] decrease in the mass variation amplitude for the shortest perturbation wavelength $\lambda = 15 \mu\text{m}$, see Fig. 6. Although we have not studied the scaling of oscillation frequencies with the perturbation wavelength [in terms of the discontinuity model of Ref. 9 and Appendix II, even the scaling of r_d with λ is not known for tailored density profiles], one can naturally expect longer perturbation wavelengths to correspond to lower frequencies. This is indeed the case. During the shock transit time, we have multiple oscillations in target 1 for $\lambda = 15 \mu\text{m}$, one full cycle for $\lambda = 30 \mu\text{m}$, and half cycle for $\lambda = 60 \mu\text{m}$. For all the other cases, we have no more than a half cycle.

Eventually, the oscillatory behavior evolves into an exponential growth for all targets. The RT exponential growth rates $\Gamma = \sqrt{gk}$ are essentially the same for all targets, since they are driven by the same ablative pressure, have the same mass, and therefore experience the same acceleration. There is, however, a significant difference between the targets in the amplitudes of these exponentially growing modes. This is precisely the difference in the seeds for RT discussed above. Firstly, we notice that the perturbations in the solid target 4 are consistently higher than in the other three. This clearly illustrates the beneficial effect of decreasing the average density of the target. The

effect has nothing to do with radiative smoothing of perturbations (recall that to emphasize this point, we have no radiation transport here), it is purely hydrodynamic, as explained in Ref. 6. Secondly, the perturbations in target 1 containing a tailored density profile are consistently lower than in the other three. Evolution of perturbations in targets 2 and 3, 4 is differently affected by the shock/rarefaction reverberations (a material interface in target 2 causes an additional shock reflection), and thereby phase-sensitive: target 2 produces, a higher or a lower RT seed than target 3 for $\lambda = 30 \mu\text{m}$ and $\lambda = 60 \mu\text{m}$, respectively, whereas for $\lambda = 15 \mu\text{m}$ both perform similarly. In contrast with this, target 1 always produces the lowest RT seed, which agrees with the results of Section II.B. The stabilizing effect of radial density tailoring is generally more effective for shorter wavelengths (at least a half cycle of oscillations has to be completed during the shock transit time, cf. Figs. 6-8), but it does not otherwise discriminate between the perturbation wavelengths. In other words, the effect is sufficiently robust.

This conclusion is confirmed by inspection of Figs. 9 to 11, plotted for a constant intensity laser drive, all the other conditions being the same as in Figs. 6 to 8, respectively. Here, acceleration of targets 2 to 4 at early time is very low. We observe oscillations due to sonic waves propagating in the lateral direction, as in the other cases of the RM-like instability development.⁵⁻⁷ Otherwise, the situation is quite similar to that presented in Figs. 6 to 8: the tailored density target 1 is consistently the best, the uniform solid target 4 is the worst, whereas the double-slab target 2 and the low-density uniform target 3 are somewhere in between, their relative performance depending on the perturbation wavelength.

Figures 12, 13 that show density perturbation maps of $\rho - \langle \rho \rangle_x$, where $\langle \rho \rangle_x$ is the average of the density over y at a given x , in targets 1 and 3 at various instants of time, help to see why the mass perturbations are lower in a target with a tailored density profile. In target 1, at early time the density perturbation is spread over a wide plasma volume. The oscillations tend to distribute the extra density more uniformly. The bubble-spike structure, distinct for a developed single mode RT instability, is only formed at late time. In target 3, the bubble-spike structure, developing from the start, oscillates as a whole. During the oscillation half cycle, the bubbles and the spikes exchange places, but they are always present. Consequently, the mass perturbations are more localized in target 3 than in target 1, and it counts when the RT growth (which is precisely the growth of localized mass perturbations) starts.

IV. CONCLUSIONS

Radial tailoring of initial density profiles in laser targets inverts the acceleration of the ablation front at early time, thereby increasing the frequency and decreasing the amplitude of its oscillations. This effect reduces the seed for the exponential RT instability growth generated by a given lateral non-uniformity in the laser drive in a target of given mass and thickness. A significant reduction in the seed mass perturbation amplitude in a target with a tailored density profile in our

simulations was found for all perturbation wavelengths, compared to a uniform target of the same mass and thickness, at the level of at least 5 or more.

The stabilizing effect of density tailoring is purely hydrodynamic. In a way, it complements a related, but different, stabilizing hydrodynamic effect of decreasing the initial density of the target, which also reduces the seed for the RT instability.⁶ If the target design includes low-density outside foam layers and more dense inner plastic or DT layers, then, as demonstrated in our simulations, a smooth transitions from low to high initial density provides a significant reduction in the RT seed compared to the case of two adjacent layers of different densities.

Our present results suggest the next step. A tailored density profile should be incorporated into a high-gain target design for direct-drive laser fusion, and an implosion of such a target should be simulated with all the relevant physics included, to see whether we could indeed expect a robust reduction in the net mass variation at stagnation. This work is now in progress.

Acknowledgments

We are grateful to Drs. S. E. Bodner and J. P. Dahlburg (NRL) for stimulating discussions. One of us (N. M.) wishes to thank Dr. Bodner and Laser Plasma Branch at NRL for their support and hospitality during the performance of this research. The work was sponsored by the U.S. Department of Energy through the contract for the Naval Research Laboratory.

Appendix I. Self-similar solution for the shock-piston flow with a tailored density profile.

Substituting the ansatz (5) into Eqs. (2)-(4) and introducing a new self-similar variable by $S(\eta) = \gamma P(\eta) / \{[\eta - U(\eta)]N(\eta)\}$, we obtain the following system of ordinary differential equations for the self-similar variables:

$$(U - \eta) \frac{d \ln N}{d\eta} + \frac{dU}{d\eta} + \chi = 0, \quad (\text{A1})$$

$$(U - \eta) \frac{d \ln S}{d\eta} + \gamma \frac{dU}{d\eta} + 1 - \frac{2}{m} = 0, \quad (\text{A2})$$

$$\frac{dU}{d\eta} = - \frac{(2m - 2 + m\chi)S + \gamma(m - 1)(U + 1)}{\gamma m(U + S - \eta)}. \quad (\text{A3})$$

Substituting (A3) into (A2), we obtain

$$\frac{d \ln S}{d\eta} = - \frac{m(\chi + 1)S + [\gamma(m - 1) + 2 - m]U + (m - 2)\eta + \gamma(m - 1)}{m(U + S - \eta)(\eta - U)}. \quad (\text{A4})$$

The two equations (A3) and (A4) must be solved numerically. Note that $N(\eta)$ does not enter Eqs. (A3)-(A4). In a general case, once a solution of Eqs. (A3), (A4) is found, $N(\eta)$ could be expressed via $U(\eta)$ and $S(\eta)$ from Eqs. (A1)-(A2) as

$$N = \text{const} \cdot S^{\frac{m(\chi+1)}{m(\gamma+1)-2}} (\eta - U)^{\frac{m(\gamma\chi-1)+2}{m(\gamma+1)-2}} \quad (\text{A5})$$

(the adiabaticity integral), where the constant is determined from the boundary conditions at the shock front. In a particular case of $m = 2/(\gamma + 1)$ (for $\gamma = 5/3$, this is our case of decelerated piston), the integral (A5) cannot be used, but instead Eq. (A2) is immediately integrated to obtain $S(\eta) = \text{const} \cdot (\eta - U)^{-\gamma}$. Then this expression for $S(\eta)$ is substituted into Eq. (A3), which must be integrated together with (A1). In either case, we have to solve two coupled ordinary differential equations.

The boundary condition at the piston, $\eta \rightarrow 0$, is $U \rightarrow 0$, hence, $S \rightarrow \infty$. Then we find from (A3) that near $\eta = 0$

$$U \sim - \frac{2m - 2 + m\chi}{\gamma m} \eta. \quad (\text{A6})$$

After the shock formation, the gas near the piston is compressed (decompressed) if the coefficient in the right-hand side of Eq. (A6) is negative (positive). Substituting (A6) into (A4), we find an asymptotic expression for $S(\eta)$:

$$S \sim S_0 \cdot \eta^{-\frac{\gamma m(\chi+1)}{(2+\gamma+\chi)m-2}}, \quad (\text{A7})$$

where S_0 is a constant to be determined. Substituting (A6) and (A7) into the integral (A5), we derive Eq. (7).

The boundary conditions at the shock front, at $\eta = \eta_s$, are the same as in Ref. 13:

$$U(\eta_s) = \frac{2\eta_s - \gamma + 1}{\gamma + 1}, \quad (\text{A8})$$

$$S(\eta_s) = \frac{2\gamma(\eta_s + 1)}{\gamma + 1}. \quad (\text{A9})$$

The self-similar coordinate of the shock front, η_s , is not known in advance. The two constants, η_s and S_0 in Eq. (A7), must be chosen to select a solution of Eqs. (A3), (A4) that satisfies two boundary conditions (A8), (A9). This is done by the shooting method. For instance, one can select a trial value of S_0 and use the asymptotic expressions (A6)-(A7) to start integration of Eqs. (A3), (A4) from some small but finite η until $U(\eta)$ equals $(2\eta - \gamma + 1)/(\gamma + 1)$ so that the boundary condition (A8) is satisfied at some value of η approximating η_s . Then we see if the left-hand side of Eq. (A9) is larger or smaller than its right-hand side, adjust the value of S_0 accordingly, and the procedure is repeated until it converges. This method was used to plot the self-similar profiles shown in Figs. 1, 2.

Appendix II. Boundary conditions at the ablation front.

We derive the boundary conditions at the ablation front for the case of time-dependent acceleration and ablation velocity, from those given in Ref. 9. Our notation is slightly different from that of Ref. 9. We suppose the plasma to be driven in the positive x direction, and the small perturbations $\propto \exp(iky)$ (the exponential factor is omitted below) to be imposed in the x - y plane. In the reference frame of the ablation front, velocity of the plasma is thus negative, equal to $-v_1$ and $-v_2$ upstream and downstream from the ablation front, respectively. By definition, $v_1 \equiv v_a$; due to mass conservation in the quasi-steady ablation front, $\rho_2 / \rho_1 = v_1 / v_2 \equiv r_D < 1$. The physical assumptions of Ref. 9 remain unchanged. Both characteristic velocities, v_1 and v_2 , are much less than the respective sound speeds; thermal conduction is strong downstream and negligible upstream, the ablation front is an isotherm. Then the linearized equations of continuity, motion, and energy yield the following boundary conditions:

$$(\rho_1 - \rho_2) \frac{d}{dt} \delta x_a = \rho_1 \delta v_{x1} - \rho_2 \delta v_{x2}, \quad (\text{A10})$$

$$\delta v_{y1} - \delta v_{y2} = -ikv_2(1 - r_D)\delta x_a, \quad (\text{A11})$$

$$\delta p_1 - \delta p_2 - 2\rho_1 v_1 (\delta v_{x1} - \delta v_{x2}) - (\rho_1 - \rho_2)g\delta x_a = 0, \quad (\text{A12})$$

$$\delta v_{x1} - \delta v_{x2} = -kv_2(1 - r_D)\delta x_a. \quad (\text{A13})$$

Here, δp , δv_x and δv_y are perturbations of pressure, axial and lateral velocity, and the subscripts 1 and 2 refer to the high-density (upstream) and low-density (downstream) plasmas separated by the ablation front, respectively. Under the assumptions outlined above, density perturbations drop out from the boundary conditions.

Substituting (A13) into (A10), we obtain Eq. (9). From (A12), (A13), we find:

$$\frac{k\delta p_1}{\rho_1} - \frac{k\delta p_2}{\rho_1} - (1 - r_D)(gk - 2k^2 v_1 v_2)\delta x_a = 0. \quad (\text{A14})$$

We have to exclude the variables referring to the downstream state. Assuming that no perturbations are incident onto the ablation front from the plasma corona (from downstream), one

can find the dependence between the downstream perturbation amplitudes

δp_2 , δv_{x2} , and δv_{y2} from the dispersion relations for the outgoing waves.⁹ After some algebra, we obtain:

$$\frac{k\delta p_2}{\rho_1} = -r_D \frac{d}{dt} \delta v_{x2} - i k v_a \delta v_{y2}. \quad (\text{A15})$$

In (A15), we express δv_{x2} from (A13), δv_{y2} from (A11), substitute the resulting expression for δp_2 into (A14), and simplify it with the aid of (9). We are left with a boundary condition that relates only the perturbations of the upstream flow variables, so that the subscript 1 in the perturbation amplitudes could be omitted:

$$\frac{k\delta p}{\rho_1} + (1 - r_D) \left[\frac{(1 - r_D)}{r_D} k^2 v_a^2 - gk \right] \delta x_a + k v_a (\delta v_x + i \delta v_y) + r_D \left(\frac{d}{dt} \delta v_x - \delta v_x \right) = 0. \quad (\text{A16})$$

This is a more general form of the boundary condition sought for. It could be used to describe the effect of perturbations incident to the ablation front from the dense plasma (in this case, δp , δv_x , and δv_y are independent variables). The stabilizing “rocket effect” of Ref. 9 is expressed by the term proportional to $k^2 v_a^2 / r_D$ in the left-hand side of Eq. (A16): a displacement δx_a of the ablation front generates a negative contribution to the pressure response $\propto -\delta x_a$ that tends to decrease the displacement.

To derive Eq. (10), we have to make an additional assumption that no perturbations are incident onto the ablation front from the upstream, thus neglecting the vorticity perturbations that arrive with the plasma particles. Then the perturbation amplitudes δp , δv_x , and δv_y are connected via the dispersion relation for sonic waves propagating upstream:

$$\frac{k\delta p}{\rho_1} = \frac{d}{dt} \delta v_x + k v_a \delta v_x, \quad \delta v_y = -i \delta v_x. \quad (\text{A17})$$

Substituting (A17) into (A16), we obtain (10).

References

- ¹ S. E. Bodner, D. G. Colombant, J. H. Gardner, R. H. Lemberg, S. P. Obenschain, L. Phillips, A. J. Schmitt, J. D. Sethian, R. L. McCrory, W. Seka, C. P. Verdon, J. P. Knauer, B. B. Afeyan, and H. Powell, *Phys. Plasmas* **5**, 1901 (1998).
- ² K. O. Mikaelian, *Phys. Rev. Lett.* **48**, 1793 (1982)
- ³ N. A. Inogamov, *Prikl. Mekh. Tekh. Fiz.* (in Russian) **5**, 110 (1985).
- ⁴ N. A. Inogamov, *JETP* **84**, 746 (1997); *Phys. Rev. E* **57**, 3352 (1998)
- ⁵ R. Ishizaki and K. Nishihara, *Phys. Rev. Lett.* **78**, 1920 (1997).
- ⁶ R. J. Taylor, A. L. Velikovich, J. P. Dahlburg, and J. H. Gardner, *Phys. Rev. Lett.* **79**, 1861 (1997); A. L. Velikovich, J. P. Dahlburg, J. H. Gardner, and R. J. Taylor, *Phys. Plasmas* **5**, 1491 (1998).
- ⁷ V.N. Goncharov, R. Betti, R.L. McCrory, C. Cherfils, *Bull. Am. Phys. Soc.* **43**, 1667 (1998); V. N. Goncharov, *Phys. Rev. Lett.*, to be published (1999).
- ⁸ J. Sanz, *Phys. Rev. Lett.* **73**, 2700 (1994).
- ⁹ A. R. Piriz, J. Sanz and F. L. Ibañez, *Phys. Plasmas* **4**, 1117 (1997).
- ¹⁰ A. L. Velikovich, F. L. Cochran, and J. Davis, *Phys. Rev. Lett.* **77**, 853 (1996); A. L. Velikovich, F. L. Cochran, J. Davis, and Y. Chong, *Phys. Plasmas* **5**, 3377 (1998).
- ¹¹ J. H. Hammer, J. L. Eddleman, P. Springer, M. Tabak, A. Toor, K. Wong, G. B. Zimmerman, C. Deeney, R. Humphreys, T. J. Nash, T. W. L. Sanford, R. B. Spielman and J. S. DeGroot, *Phys. Plasmas* **3**, 2063 (1996).
- ¹² N. A. Krasheninnikova, *Izv. Akad. Nauk SSSR, Otd. Tekh. Nauk* **8**, 22 (1955) (in Russian); a brief description of this solution and references to subsequent Russian publications are given by L. I. Sedov, *Similarity and Dimensional Methods in Mechanics* (CRC Press, Boca Raton, 1993), Chap. IV, Sec. 6.
- ¹³ S. M. Gol'berg and A. L. Velikovich, *Phys. Fluids B* **5**, 1164 (1993).
- ¹⁴ R. L. McCrory, L. Montierth, R. L. Morse, and C. P. Verdon, in *Laser Interaction and Related Plasma Phenomena* (Plenum, New York, 1981), Vol. 5, pp. 713-742; R. Betti, R. L. McCrory, and C. P. Verdon, *Phys. Rev. Lett.* **71**, 3131 (1993).
- ¹⁵ L. J. Slater, "Confluent Hypergeometric Functions", in *Handbook of Mathematical Functions*, ed. by M. Abramowitz and I. A. Stegun (Dover, New York, 1972), pp. 503-536.
- ¹⁶ V. N. Goncharov, R. Betti, R. L. McCrory, P. Sorotokin, and C. P. Verdon, *Phys. Plasmas* **3**, 1402 (1996).
- ¹⁷ S. E. Bodner, *Phys. Rev. Lett.* **33**, 761 (1974).
- ¹⁸ N. C. Freeman, *Proc. Roy. Soc. A* **228**, 341 (1955); P. M. Zaidel, *J. Appl. Math. Mech.* **24**, 316 (1960).

- ¹⁹ M. H. Emery, J. H. Gardner, and J. P. Boris, Appl. Phys. Lett. **41**, 808 (1982).
- ²⁰ E. S. Oran and J. P. Boris, *Numerical Simulations of Reactive Flow* (Elsevier, New York, 1987), and references therein.
- ²¹ F. F. Grinstein, and C. R. DeVore, Phys. Fluids **8**, 1237 (1996).
- ²² A. M. Landsberg, J. P. Boris, W. Sandberg, and T. R. Young, Jr., AIAA Paper 95-0047, American Institute of Aeronautics and Astronautics, Reston, VA 20101-4344, January 1995.
- ²³ J. H. Gardner, S. E. Bodner, and J. P. Dahlburg, Phys. Fluids B **3**, 1070 (1991).
- ²⁴ R. J. Taylor, J. P. Dahlburg, A. Iwase, J. H. Gardner, D. E. Fyfe, and O. Willi, Phys. Rev. Lett. **76**, 1643 (1996); C. J. Pawley, K. Gerber, R. H. Lehmberg, E. A. McLean, A. N. Mostovych, S. P. Obenschain, J. D. Sethian, V. Serlin, J. A. Stamper, C. A. Sullivan, S. E. Bodner, D. Colombant, J. P. Dahlburg, A. J. Schmitt, J. H. Gardner, C. Brown, J. F. Seely, T. Lehecka, Y. Aglitskiy, A. V. Deniz, Y. Chan, N. Metzler, and M. Klapisch, Phys. Plasmas **4**, 1969 (1997).
- ²⁵ J. P. Boris and D. L. Book, J. Comput. Phys. **11**, 38 (1973), also see “Solution of the Continuity Equation by the Method of Flux-Corrected Transport,” *Methods in Computational Physics*, v. 16 (Academic Press, New York, 1976), pp. 85-129.
- ²⁶ L. Spitzer and R. Härm, Phys. Rev. **89**, 977 (1953).
- ²⁷ S. E. Bodner, D. Colombant, K. Gerber, R. H. Lehmberg, E. A. McLean, A. N. Mostovych, M. S. Pronko, C. J. Pawley, A. J. Schmitt, J. D. Sethian, V. Serlin, J. A. Stamper, C. A. Sullivan, J. P. Dahlburg, J. H. Gardner, Y. Chan, A. V. Deniz, J. Hardgrove, T. Lehecka, and M. Klapisch, Phys. Plasmas **3**, 2098 (1996).

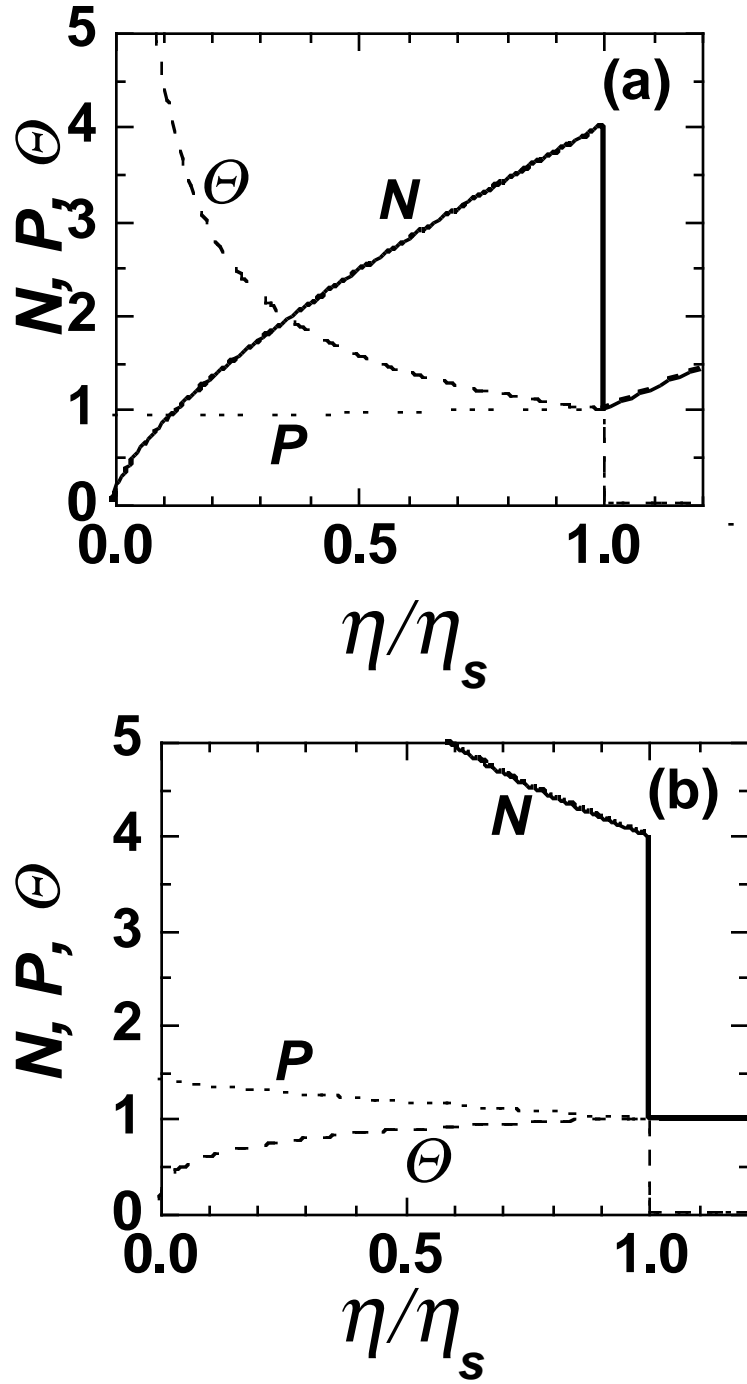


Fig. 1. Self-similar profiles of density N (thick lines), pressure P and temperature Θ for the shock-piston flows driven by a linearly rising pressure (the self-similar coordinate η is normalized with respect to the shock coordinate, η_s): (a) tailored (parabolic) initial density profile ($\chi = 2$), deceleration ($m = 3/4$); (b) uniform density profile ($\chi = 0$), acceleration ($m = 3/2$).

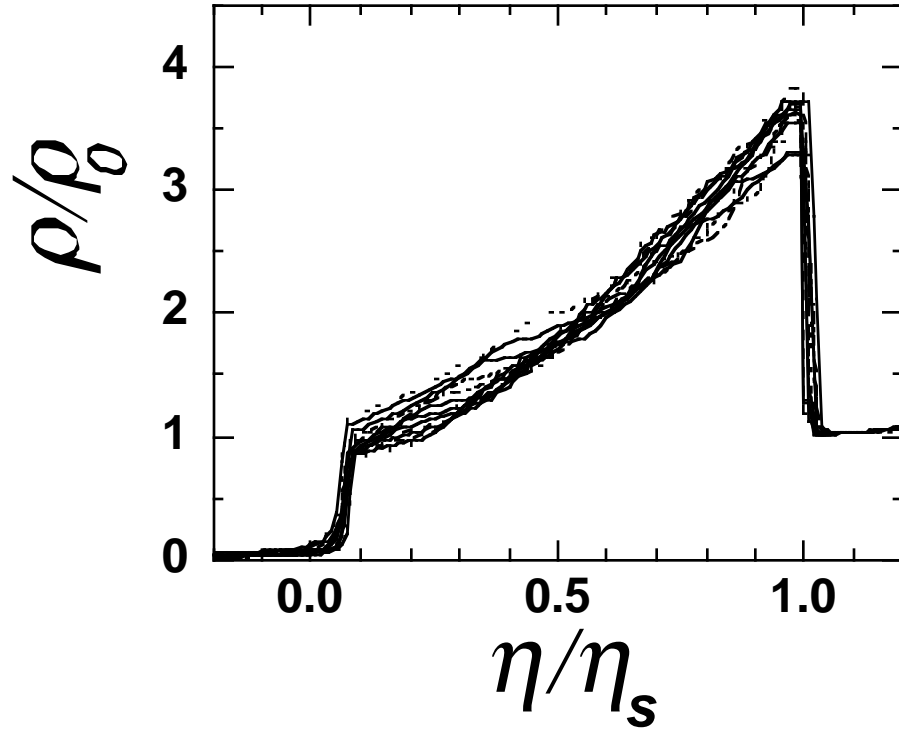


Fig. 2. Self-similar density profile of Fig. 1(a) (thick solid curve) compared to the density profiles obtained in a simulated ablatively driven shock-piston flow that approximately corresponds to the same parameters ($\chi = 2$, $m = 3/4$). Simulation results (13 thin solid and dotted curves) are calculated during the shock transit time for this target, between 1.5 and 3.5 ns. The flow profiles are seen to be approximately self-similar.

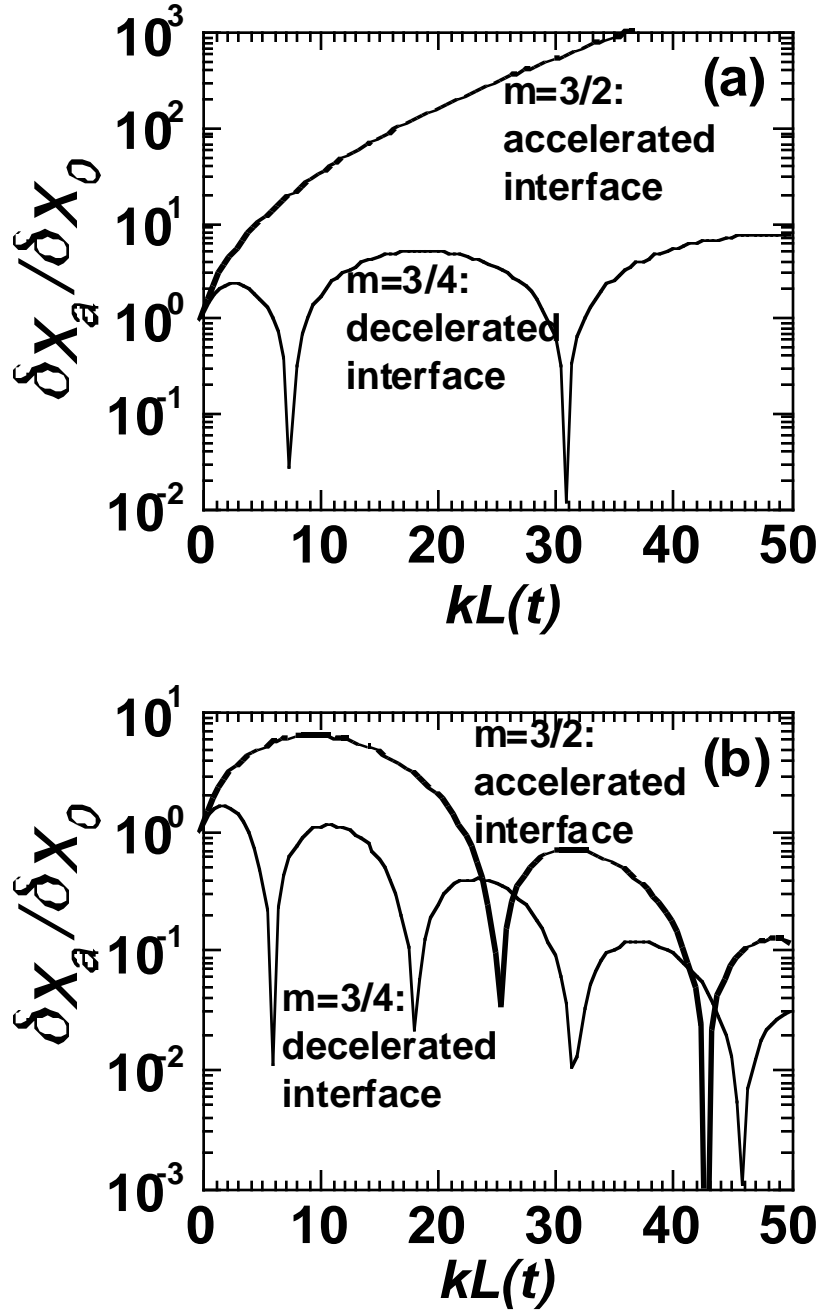


Fig. 3. Evolution of perturbations of the ablation front given by (13) for $r_D = 0.05$, $A = 0.9$, $m = 3/4$ and $m = 3/2$ (thin and thick solid curves, respectively): (a) no mass ablation, $v = 0$; (b) with mass ablation, $v = 0.05$.

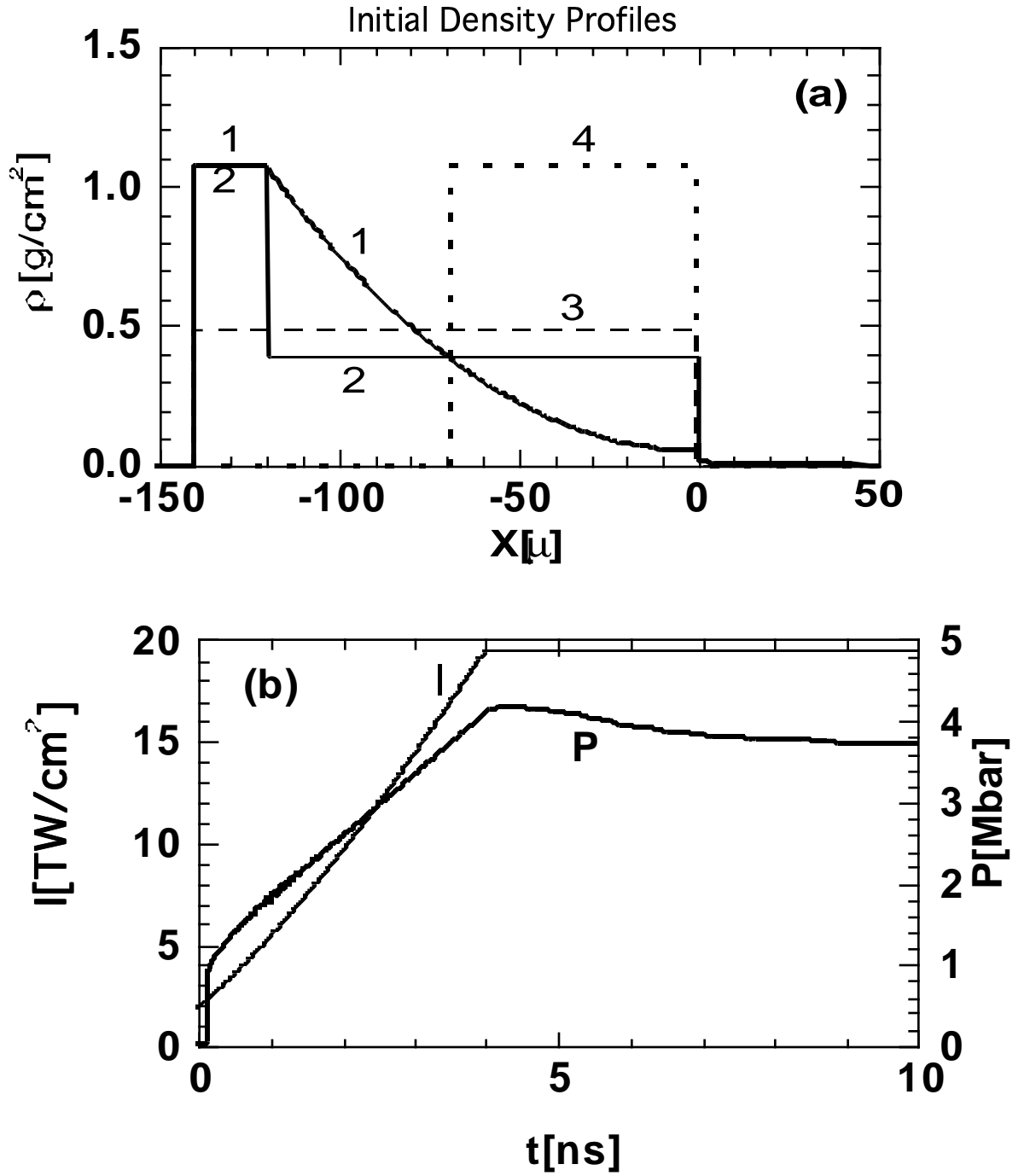


Fig. 4. (a) Initial density profiles in targets: parabolic (1) and low-density uniform (2) profiles followed by a solid payload; all-uniform low-density (3) and solid plastic density (4) profiles. (b) Laser pulse shape selected to make ablative pressure increase linearly with time from $t_1 = 0.2$ ns to $t_2 = 4$ ns: $p \propto I^\alpha$, where $\alpha = 0.75$, so we choose $I(t) = \{I_1^\alpha(t_2 - t) + I_2^\alpha(t - t_1)\}^{1/\alpha}$, where $I_1 = 3 \cdot 10^{12} \text{ W/cm}^2$ and $I_2 = 1.9 \cdot 10^{13} \text{ W/cm}^2$. The pressure rise is indeed approximately linear in time.

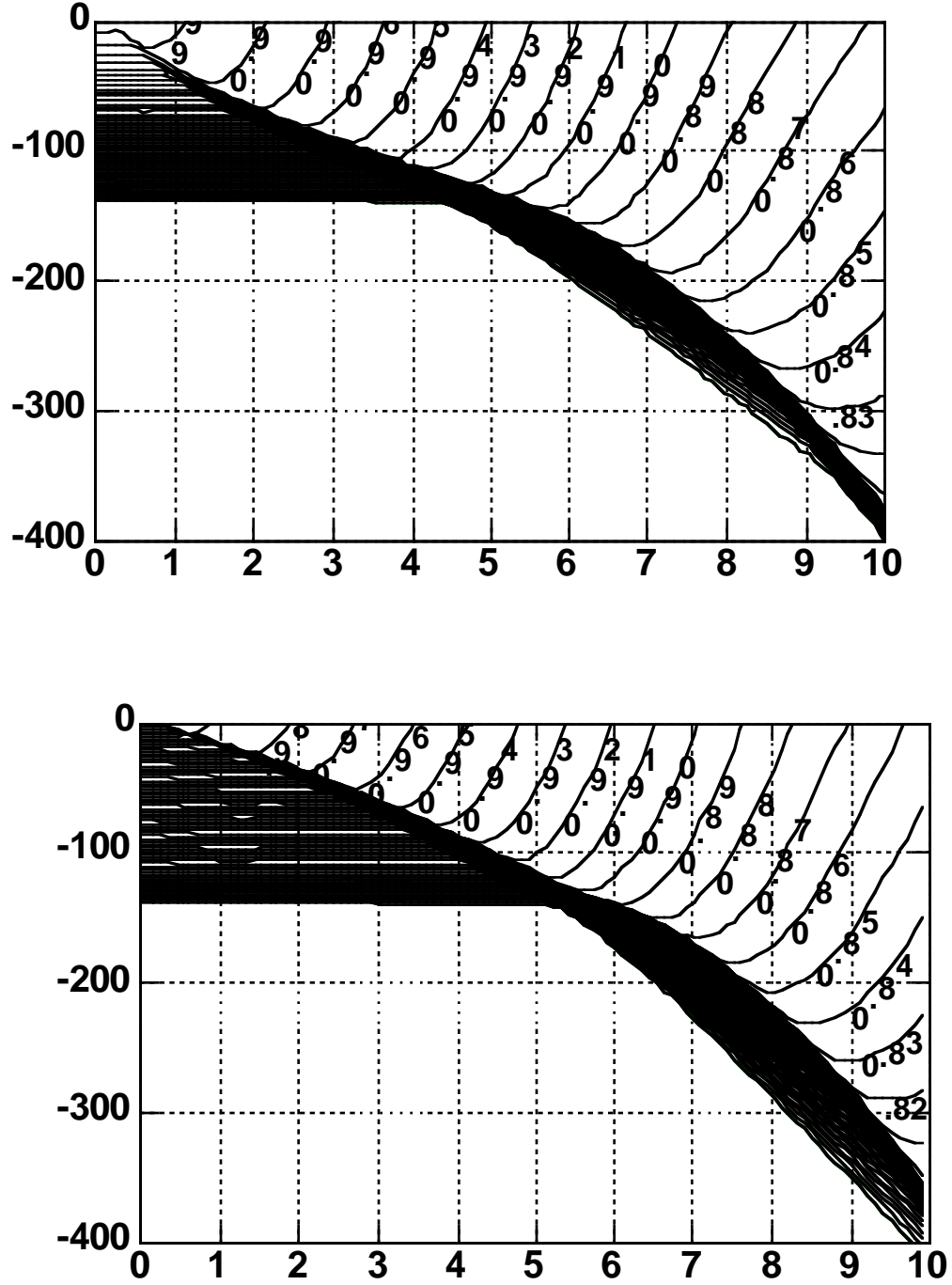


Fig. 5. x - t diagrams for plasma particles labeled by their initial mass coordinates for: (a) target 1 with a parabolic density profile; (b) target 2 with a low-density uniform profile; both followed by a solid density payload. The upper envelope curve of the high-density area is the ablation front. At early time, in the parabolic density target, this curve is convex, which implies deceleration.

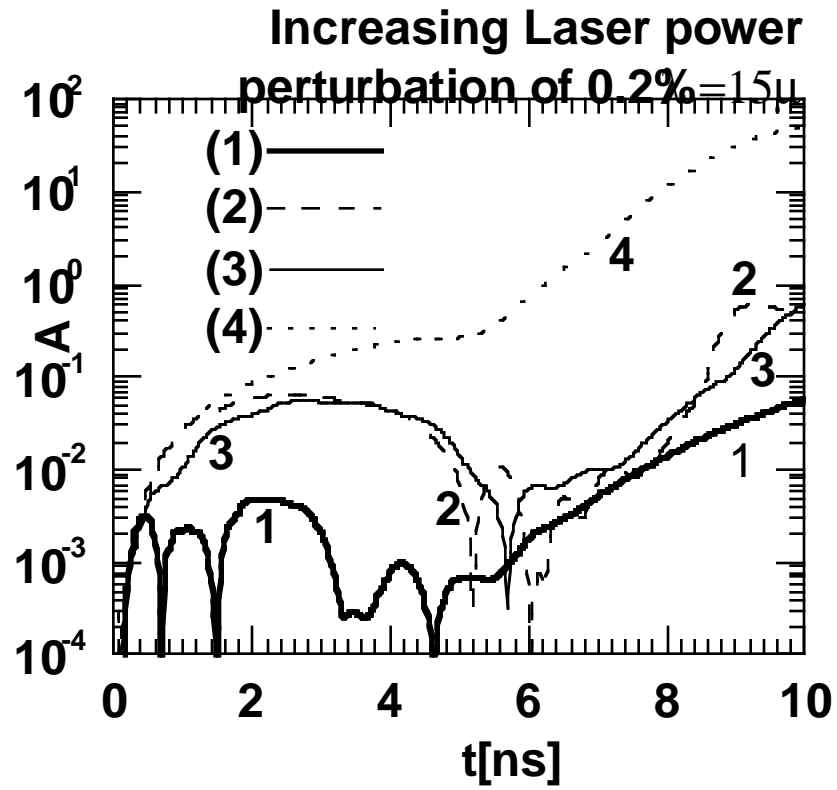


Fig. 6. Time evolution of areal mass variation ($\mu\text{m}\xi\text{g}/\text{cm}^3$) in targets 1 to 4 driven by the laser pulse of Fig. 4(b), with a 0.2% rms single-mode lateral intensity variation at $\lambda = 15 \mu\text{m}$.

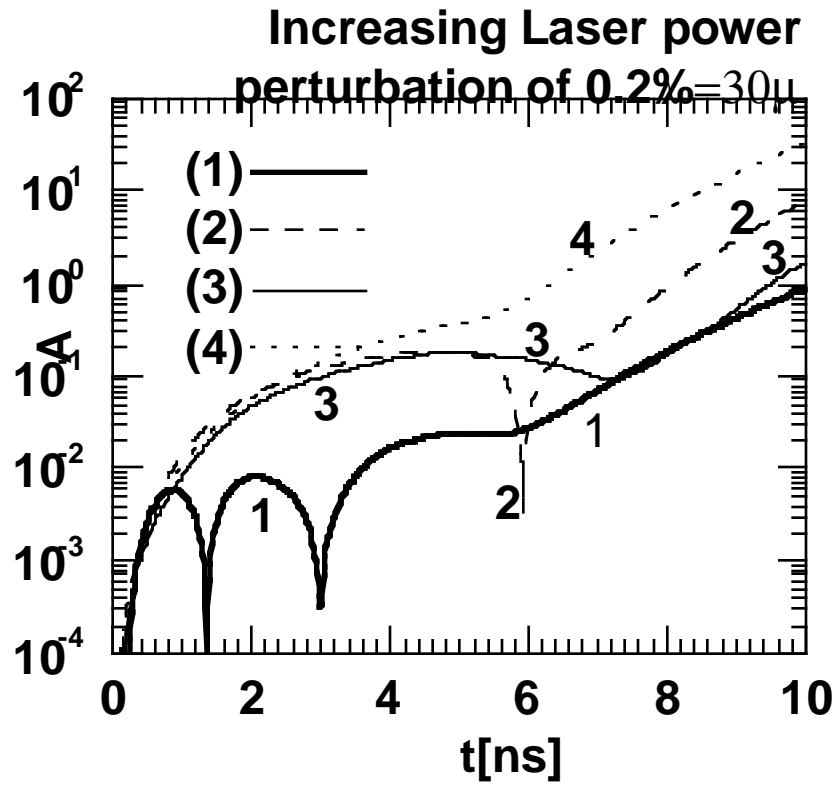


Fig. 7. Time evolution of areal mass variation ($\mu\text{m}\xi\text{g}/\text{cm}^3$) in targets 1 to 4 driven by the laser pulse of Fig. 4(b), with a 0.2% rms single-mode lateral intensity variation at $\lambda = 30 \mu\text{m}$.

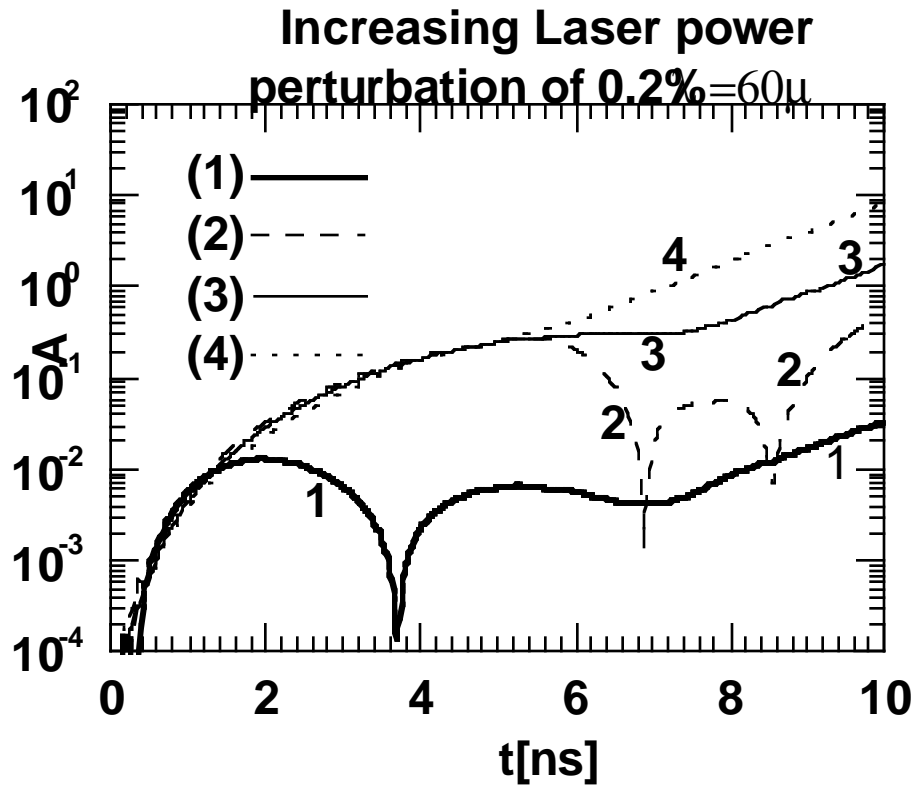


Fig. 8. Time evolution of areal mass variation ($\mu\text{m}\xi\text{g}/\text{cm}^3$) in targets 1 to 4 driven by the laser pulse of Fig. 4(b), with a 0.2% rms single-mode lateral intensity variation at $\lambda = 60 \mu\text{m}$.

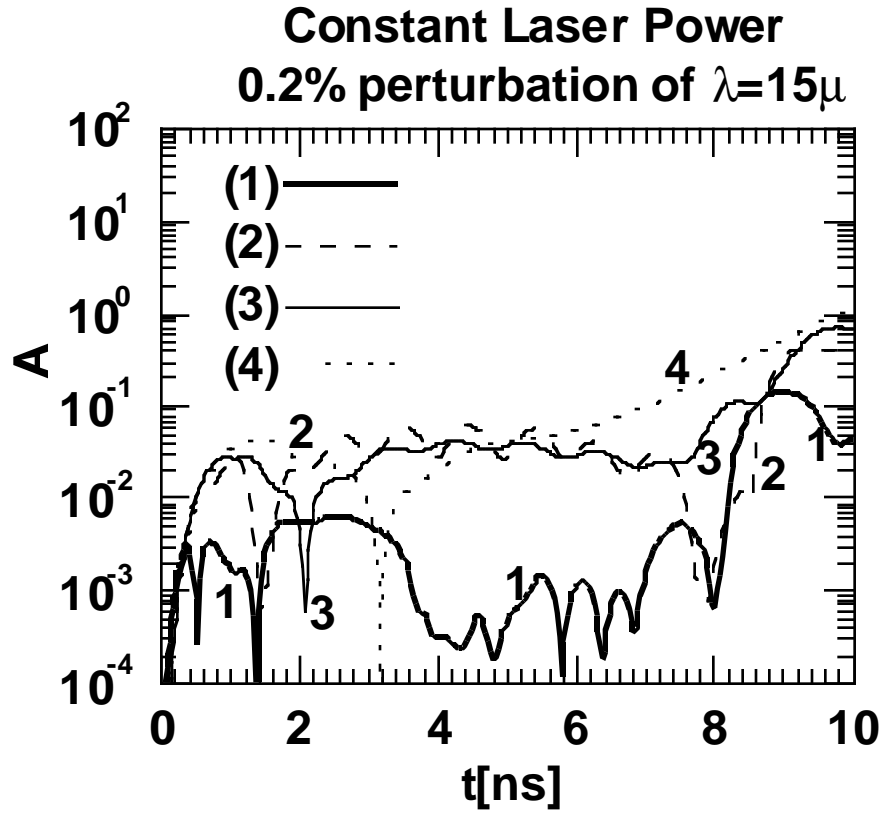


Fig. 9. Time evolution of areal mass variation ($\mu\text{m}\xi\text{g}/\text{cm}^3$) in targets 1 to 4 driven by the laser pulse of constant intensity, with a 0.2% rms single-mode lateral intensity variation at $\lambda = 15 \mu\text{m}$.

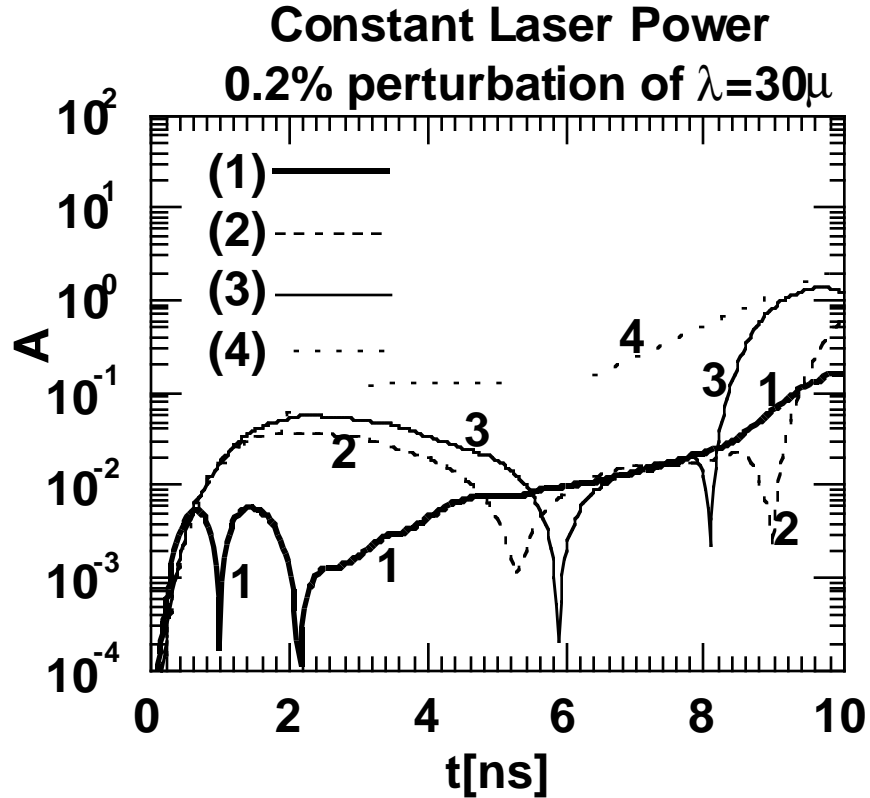


Fig. 10. Time evolution of areal mass variation ($\mu\text{m}\xi\text{g}/\text{cm}^3$) in targets 1 to 4 driven by the laser pulse of constant intensity, with a 0.2% rms single-mode lateral intensity variation at $\lambda = 30 \mu\text{m}$.

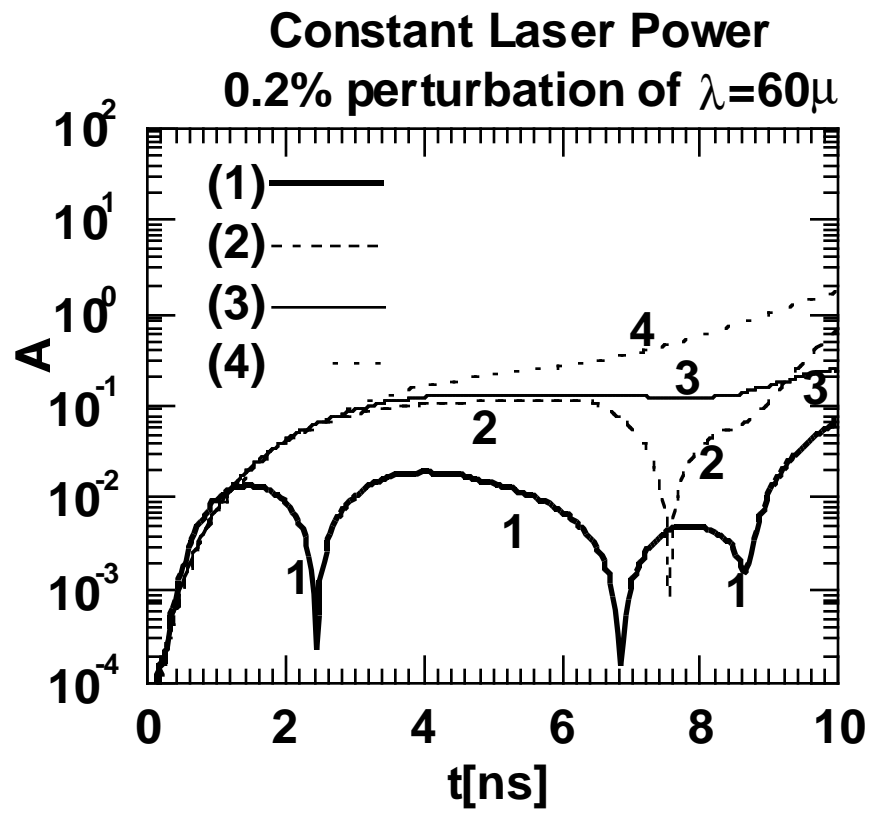


Fig. 11. Time evolution of areal mass variation ($\mu\text{m}\xi\text{g}/\text{cm}^3$) in targets 1 to 4 driven by the laser pulse of constant intensity, with a 0.2% rms single-mode lateral intensity variation at $\lambda = 60\mu\text{m}$.

Parabolic Density; $\lambda=15\mu$ Laser Perturbation

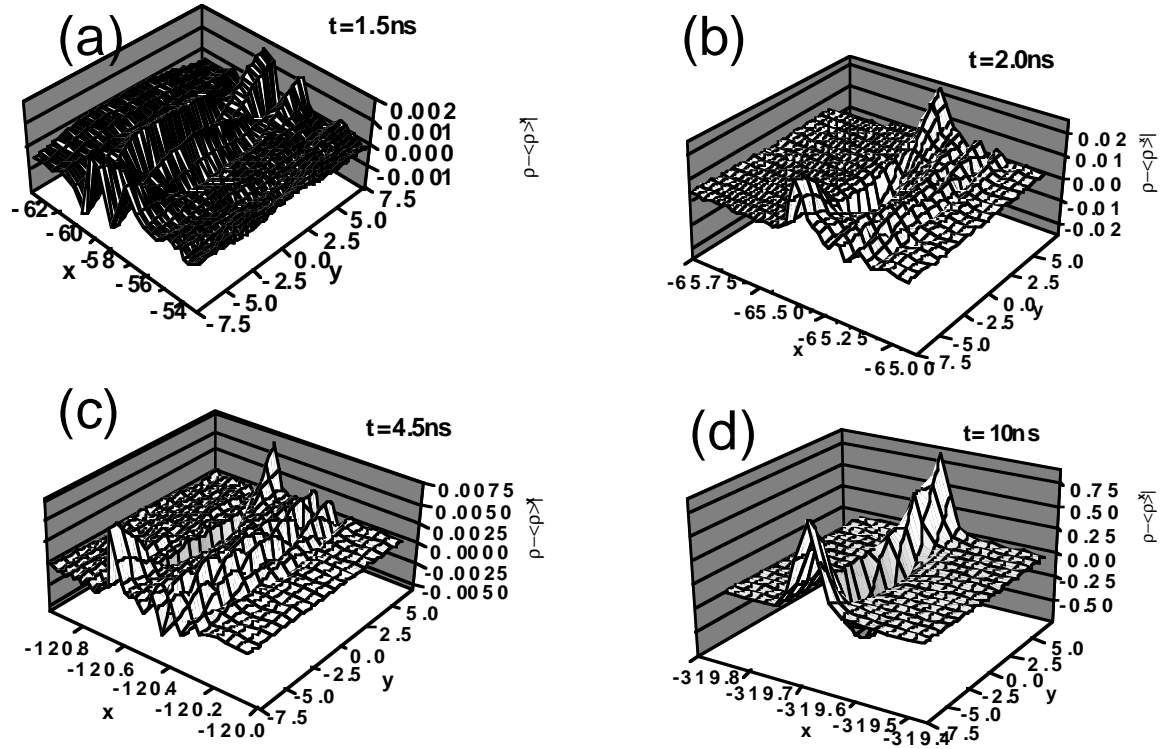


Fig. 12. Density perturbation maps of $\rho - \langle \rho \rangle_x$ in a tailored density target 1 driven by a laser pulse of Fig. 4(b) with a 15μ perturbation wavelength at different times: (a) 1.5 ns; (b) 2 ns; (c) 4.5 ns; (d) 10 ns.

Constant Density; $\lambda=15\mu$ Laser Perturbation

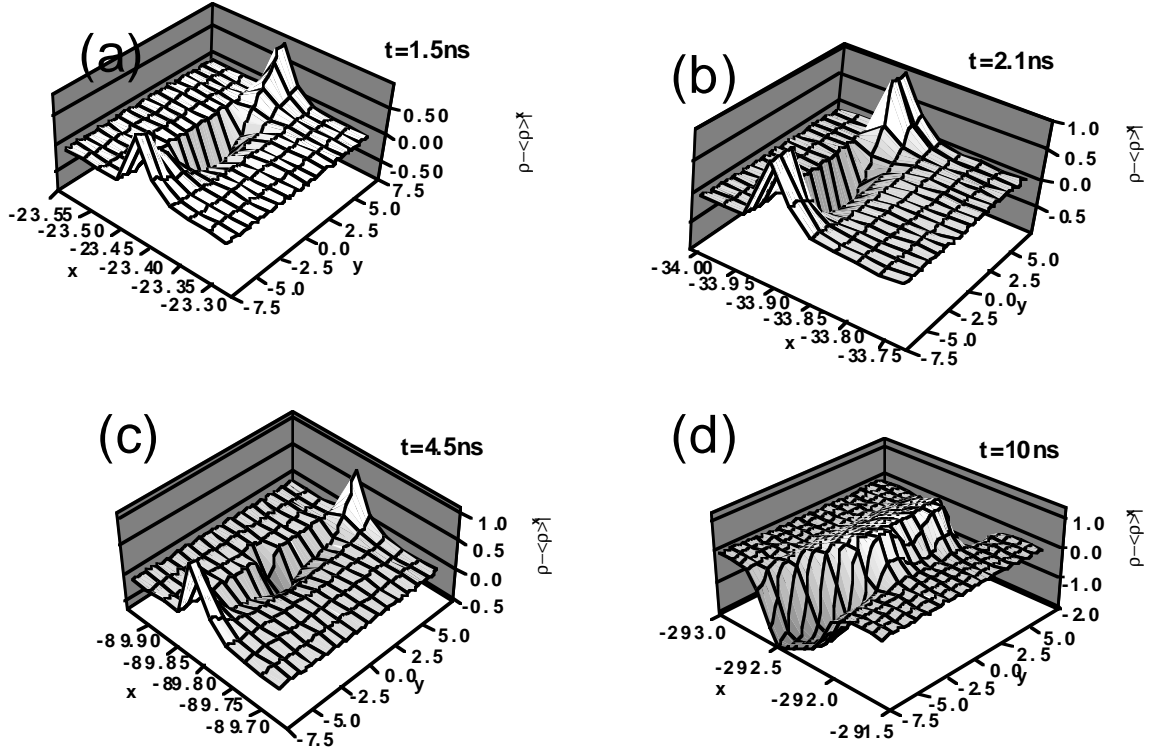


Fig. 13. Density perturbation maps of $\rho - \langle \rho \rangle_x$ in a uniform density target 3 driven by a laser pulse of Fig. 4(b) with a 15μ perturbation wavelength at different times: (a) 1.5 ns; (b) 2 ns; (c) 4.5 ns; (d) 10 ns.